Journal of Thermal Analysis and Calorimetry, September 2022 (early Access)
doi.org/10.1007/s10973-022-11562-7

Calorimetry characterization and crystallization modelling of wax-based mixtures under isokinetic and non-isokinetic cooling

Han WANG[1,2], Michel BELLET[1], Séverine A.E. BOYER[1], Florence DALLE[2]

[1]MINES ParisTech – PSL Research University, CEMEF – Centre de Mise en Forme des Matériaux, UMR CNRS 7635, CS 10207, 06904 Sophia Antipolis, France

[2]Parfums Christian Dior, 185 Avenue de Verdun, 45800 Saint-Jean-de-Braye, France

Abstract

Characterization and modelling of wax crystallization must be carefully addressing to understand wax-oil organogels formation. During casting process of wax-based mixtures, wax crystallization occurs under concomitant non-constant and high cooling rates. In this study, the crystallization kinetics of two representative wax-based materials was studied by power-compensated Differential Scanning Calorimetry (DSC) with moderate-high cooling rates (from -20 to -200 °C min^{-1}) in constant cooling rates (isokinetic) conditions and simplified non-constant cooling rate (non-isokinetic) conditions. Analyses based on the evolution of the mass fraction of solid wax calculated from heat flow (DSC signal) show similar kinetics trend and enthalpy of crystallization for the different isokinetic conditions, but with a significant influence on the supercooling effects. Considering the limits of the classic Avrami kinetics modelling for high aspect ratio crystals and complex mixtures, a semi-empirical modelling approach of non-isokinetic cooling conditions on a differential form is proposed. The modelling shows a good correlation with experimental results.

Keywords

Wax-oil organogels; Differential Scanning Calorimetry; Crystallization kinetics modelling; Isokinetic and non-isokinetic cooling

1. Introduction

Waxes are organic semi-crystalline thermoplastics comprised of fatty hydrocarbons and their derivatives. An exact description of chemical composition of waxes is difficult because they are usually mixtures of alkanes, fatty alcohols, fatty esters, or other organic components with different molecular weights. Polymethylene chain structure is generally present in most wax molecules. Below the wax crystallization temperature, subunits of methylene group -CH_2- organize into an ordered crystalline structure [1]. From a melted binary wax-oil mixture, wax crystallization upon cooling results in a semi-solid paste, even with very low wax quantity in some cases [2-4]. The microstructure of the solidified mixture shows an interconnected three-dimensional skeleton of wax crystals in which is entrapped a continuous oil phase [5, 6]. These wax-based mixtures are categorized as "organogels" (or "oleogels"), and their solidification process is no other than a gelation [7]. Wax-oil organogels can be used as structuring agents for potential substitutions to saturated fatty acids in food shortenings [6] or make-up products [8], for example, lipsticks that can be considered as organogels from 50 wt% to nearly 100 wt% of waxes and oils. In a very different context, during crude oil extraction and transport, the formation of paraffin organogels and their deposition along pipeline walls, especially in cold weather conditions, is undesired as the gelation can lead to significantly higher pressure drops, or even pipeline blockage [9].

Several previous studies have demonstrated significant influences of thermomechanical conditions on microstructural and rheological aspects for wax-based mixtures [4, 10-14], and such investigations are important to control various industrial processes. For example, the temperature gradient and the shear conditions can influence the crystallization kinetics as well as microstructural and rheological features of wax deposition in crude oil pipelines [2, 9, 12]. In food science, the cooling and shear rates are used as actuators to control mechanical properties of edible waxy organogels [4, 15].

Similarly, thermomechanical parameters are considered critical in the casting of cosmetic products, especially lipsticks. The overall crystallization kinetics determines the ratio of solidified phase and impacts eventually the mechanical properties of the material. Identifying the crystallization kinetics upon processing becomes thus critical. However, the characterization of wax crystallization kinetics in conditions of lipstick casting is challenging. It should be noted that in most previous studies on wax-oil organogels, cooling rates were generally lower than -20 °C min^{-1} and were kept constant (*isokinetic* conditions), but they can be much higher and non-constant during casting process. In industrial casting conditions, when the melted liquid lipstick paste (at about 100 °C) is poured into a cold mold (at around 20 °C), cooling is very rapid at the paste-mold interface, while it takes several minutes for the lipstick center to approach the mold temperature. During the solidification process, the cooling rate is thus generally higher than -20 °C min^{-1} at the center of the lipstick and increases along the radius, up to the surface. Moreover, the cooling rate is variable (*non-isokinetic* conditions). To our knowledge, there are yet few studies on wax crystallization kinetics under rapid and non-isokinetic cooling conditions.

Experimentally, Differential Scanning Calorimetry (DSC) is often used to characterize crystallization kinetics (overall kinetics) for crystalline or semicrystalline materials [16], such as polymers [17-20],

metals [21], petroleum products [22, 23, 24], cosmetics [25], and fatty materials [26, 27]. Small DSC sample size enables a short thermal response time and high cooling rates. From the specific thermal signal caused by crystallization, a precise description of crystallization kinetics can be obtained. For wax-based mixtures, on one hand, DSC scans allow evaluating the impact of cooling rate on wax appearance temperature T_{WA}, or WAT, the temperature at which wax crystallization starts. Several studies have shown that there is a linear correlation between the temperature T_{WA} and the cooling rate $\dot{T}$: $T_{WA}(\dot{T}) = a_0 + a_1\dot{T}$, where a_0 and a_1 are constant coefficients [11, 22, 24]. While other studies suggested a quadratic correlation $T_{WA}(\dot{T}) = b_0 + b_1\dot{T} + b_2\dot{T}^2$ [12, 28, 29], where b_0, b_1 and b_2 are constant coefficients. On the other hand, the heat flow integration of thermal signals on a DSC scan quantifies the crystallization advancement for further modelling of kinetics [30] or thermodynamics [24].

Classic kinetics models based on Avrami theory have been widely exploited for modelling nucleation and growth of various materials in isothermal conditions [26, 31-33]. Within studies to approach to non-isothermal conditions, Nakamura et al. proposed an expansion of the isothermal Avrami modelling to non-isothermal conditions [34]. Ozawa also developed a non-isothermal modelling for constant cooling rate measurements [35] and Billon et al. proposed the application to non-constant rate cooling conditions [36]. Classic nucleation and growth theories may encounter large errors with high aspect ratio and anisotropic crystalline growth [37, 38], which indicates possible errors when using classic kinetics model for wax crystallization because of needle-like or platelet-like wax crystals [9, 39]. Moreover, commercialized wax and wax-based mixtures can be very different in terms of multiple wax components. Crystallization modelling from DSC thermal signals without detailing each component is thus desired.

In this study, a characterization methodology following by a semi-empirical modification of the Avrami theory are suggested. This approach is suitable for modelling wax crystallization in complex mixtures in moderate-high cooling rate and non-isokinetic conditions. Followingly, in **Section 2**, the Avrami theory will be briefly reviewed and discussed. Experimentally, **Section 3** will provide a method to exploit the experimental thermal signal of wax crystallization in terms of kinetics variables. In **Section 4**, the experimental protocols of wax crystallization characterization on isokinetic and non-isokinetic conditions will be discussed. The characterization results of two representative wax-oil mixture samples will be shown in **Section 5**. In **Section 6**, we will study kinetics modelling for both isokinetic and non-isokinetic conditions. For isokinetic modelling, several limits of classic kinetics Ozawa model will be discussed. Instead, a semi-empirical model will be proposed based on characterization results and will be further examined by comparison to experimental results for both isokinetic and non-isokinetic conditions.

2. Classic kinetics models

The Avrami theory is often used for isothermal kinetics modelling of crystallization [31]. Kinetics calculations are based on the volume fraction of the crystallized solid phase f_v, and on the "overlap" of

crystalline entities. f_v is a value ranging from 0 to 1 during crystallization. In a general form of the Avrami model, the volume fraction of crystallization should satisfy:

$$f_v(t) = 1 - exp(-Kt^n) \quad \textbf{(1)}$$

where K is a constant which only depends on temperature T, and n is the Avrami coefficient. n is dimensionless and depends on nucleation and entities growth conditions. For example, under instantaneous nucleation, n takes the value of 3 for three-dimensional growth, 2 for two-dimensional growth, and 1 for one-dimensional growth.

Nakamura et al. consider an arbitrary thermal path as numbers of isothermal steps [34]. They expanded the Avrami model to non-isothermal conditions, with the following form:

$$f_v(t) = 1 - exp\left[-\left(\int_0^t K(T)d\tau\right)^n\right] \quad \textbf{(2)}$$

To take account of the induction time in non-isothermal conditions, Scheil suggested the following criterion to calculate non-isothermal induction time t_{ind} from isothermal induction times $t_{ind}^{iso}(T)$ [40]; Chan and Isayev introduced this definition into polymer crystallization [41]:

$$\int_0^{t_{ind}} \frac{dt}{t_{ind}^{iso}(T)} = 1 \quad \textbf{(3)}$$

Based on the Avrami theory, another approach for non-isothermal conditions is proposed by Ozawa for constant cooling rate conditions [35]:

$$f_v(T, \dot{T}) = 1 - exp\left(-\frac{\chi(T)}{|\dot{T}|^n}\right) \quad \textbf{(4)}$$

where $\dot{T}$ is the cooling rate dT/dt (unit: °C min^{-1}); $\chi(T)$ is a function which only depends on temperature T. In a double logarithm plot associated with equation **(4)**, the slope can be attributed to the Avrami coefficient n, and $ln(\chi(T))$ can be assigned with a fitting function.

Accordingly, Billon et al. suggested a generalization of the Ozawa equation **(4)** for non-constant cooling rate conditions by incremental calculations [36]:

$$f_v(t^N) = 1 - exp\left(-\left(\sum_{j=1}^{N} \frac{1}{|\dot{T}^j|}\left(\chi^{\frac{1}{n}}(T^j) - \chi^{\frac{1}{n}}(T^{j-1})\right)\right)^n\right) \quad \textbf{(5)}$$

where t^N is the current time increment and j represents the increment index of time steps.

Experimentally, isothermal tests are used for modelling with Avrami equation **(1)**, while constant cooling rate tests are used with Ozawa form **(4)**, which is preferred for materials with rapid crystallization. Direct observation of crystallization by optical microscopy or indirect measurement such as DSC scans or density measurements can be used to approach the evolution of the volume

fraction $f_v(t)$ or $f_v(T,\dot{T})$. In this study, DSC scans with isokinetic and non-isokinetic cooling conditions have been chosen to characterize wax crystallization kinetics.

3. Kinetics characterization strategy by DSC

3.1. Isokinetic cooling conditions

The principle of a DSC characterization is to measure the necessary heat power difference to maintain the sample and a reference at nearly the same temperature during a preset temperature profile. By convention, a DSC diagram presents the measured heat power difference versus temperature. This heat power difference is named as "heat flow" (noted as Φ_s, unit: mW). Heat-flux DSC and power-compensated DSC are two methods to measure the heat flow. In this study, we choose a power-compensation DSC which directly measures the heat power difference of a sample and a reference in two twin mini-furnaces. Ideally, heat flow should be constant during a temperature scan, if the specific heat of the sample is constant and there is no phase transformation. However, an existing asymmetry of the heat control or a difference in the specific heat between the two mini ovens introduces usually a non-flat baseline. Moreover, the absolute value of heat flow signal Φ_s is proportional to the cooling rate and to the sample mass for each individual scan, which leads to non-comparable phase transformation thermal signals for different cooling rates.

Therefore, a post-processing protocol of heat flow data has been introduced in this work. As shown in **Fig. 1a**, heat flow indicates a phase transformation phenomenon from temperature T_{tr}^{i} to T_{tr}^{f}. A heat flow baseline is manually chosen on two smooth sections without transformational heat, from T_{DSC}^{i} to T_{tr}^{i} and from T_{tr}^{f} to T_{DSC}^{f}. In the case of cooling scans, T_{WA} is equivalent to the on-set temperature of the crystallization signal T_{tr}^{i}. The baseline can be completed with a spline interpolation inside the transformation zone, noted as Φ_b (unit: mW). The heat flow of the phase transformation can then be normalized by $\dot{T}$ and the sample mass m (unit: mg), into a specific heat of phase transformation, denoted as c_p^{tr} (unit: J g^{-1} K^{-1}):

$$c_p^{tr} = \frac{\Phi_s - \Phi_b}{m\dot{T}} \qquad \textbf{(6)}$$

c_p^{tr} is positive under both heating and cooling conditions. Instead of heat flow Φ_s, the transformational specific heat c_p^{tr} will be used for further comparisons.

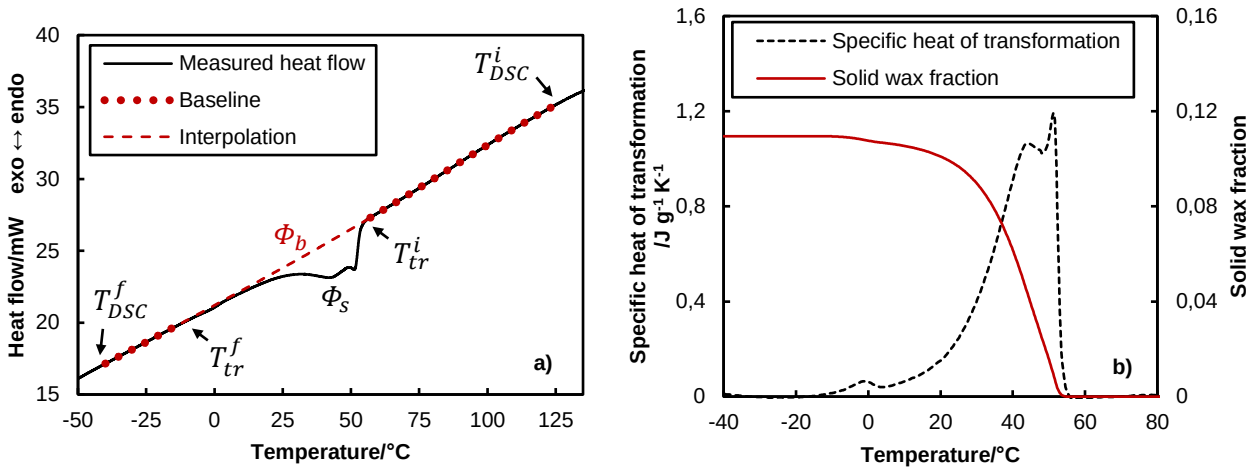

Fig. 1 a Baseline interpolation of a phase transformation measured by a power compensated DSC (cooling starts from the right side of the diagram) **b** Transformational specific heat c_p^{tr} and solid wax fraction f_{SW}, calculated with the proposed baseline interpolation and enthalpy integration

The enthalpy of phase transformation ΔH_{tr} (unit: J g^{-1}) can be integrated in the transformation zone, from T_{tr}^i to T_{tr}^f:

$$\Delta H_{tr} = \int_{T_{tr}^i}^{T_{tr}^f} c_p^{tr}\, dT \qquad \textbf{(7)}$$

A negative value of enthalpy signifies that the phase transformation is exothermic. On cooling scans, ΔH_{tr} is the total enthalpy of crystallization.

We define here *solid wax fraction* f_{SW} as a mass fraction to represent the quantity of semi-crystalline phase. The value of f_{SW} is the cumulated enthalpy (integration of c_p^{tr} from T_{WA} to T) divided by a reference enthalpy ΔH_{ref}:

$$f_{SW}(T) = \frac{\int_{T_{WA}}^{T} c_p^{tr}\, dT}{\Delta H_{ref}} \qquad \textbf{(8)}$$

An example of as-calculated c_p^{tr} and f_{SW} can be seen in **Fig. 1b**. As for the reference enthalpy ΔH_{ref}, it is defined as the mass-weighted average of enthalpies of crystallization ΔH_{tr}^k of each wax component k (with mass fraction w^k) of the wax-based material:

$$\Delta H_{ref} = \frac{\sum_k w^k \Delta H_{tr}^k}{\sum_k w^k} \qquad \textbf{(9)}$$

With this definition of ΔH_{ref}, f_{SW} increases from 0 to 1 for cooling of a single wax component from liquid melt; when cooling a wax-based mixture, f_{SW} increases from 0 to a final value of f_{SW}^{max} (smaller than 1). The f_{SW} should not be confused with the degree of crystallinity, often used in polymer crystallization. It should also be noted that f_{SW} is a global approximation of crystallization of each wax

component. A more precise determination of solid phase fraction should be feasible via other characterization methods such as pulsed Nuclear Magnetic Resonance (p-NMR) [42] but will be not discussed in this study. Since the densities of wax and oil components are close (approximatively 0.9 g cm^{-3} at room temperature), the mass fraction f_{SW} is thus comparable to the volume fraction f_v that is used in the Avrami theory. In our study, f_{SW} is used to describe crystallization kinetics and modelling.

3.2. Non-isokinetic cooling conditions

Experimentally, applying a thermally controlled non-isokinetic temperature program is a challenge for most commercialized DSC calorimeters. In our study, DSC scans have been conducted with simplified non-isokinetic cooling conditions: in two sections, constant cooling programs are applied with different cooling rates $\dot{T}_1$ and $\dot{T}_2$, the cooling rate change taking place at temperature T^*. In our study, we suppose that the two cooling rates satisfy $|\dot{T}_1| > |\dot{T}_2|$, referring to a monotonic decreasing cooling rate, as in many process conditions. For simplification reasons, a non-isokinetic cooling scan will be noted as "$|\dot{T}_1|$-$|\dot{T}_2|$".

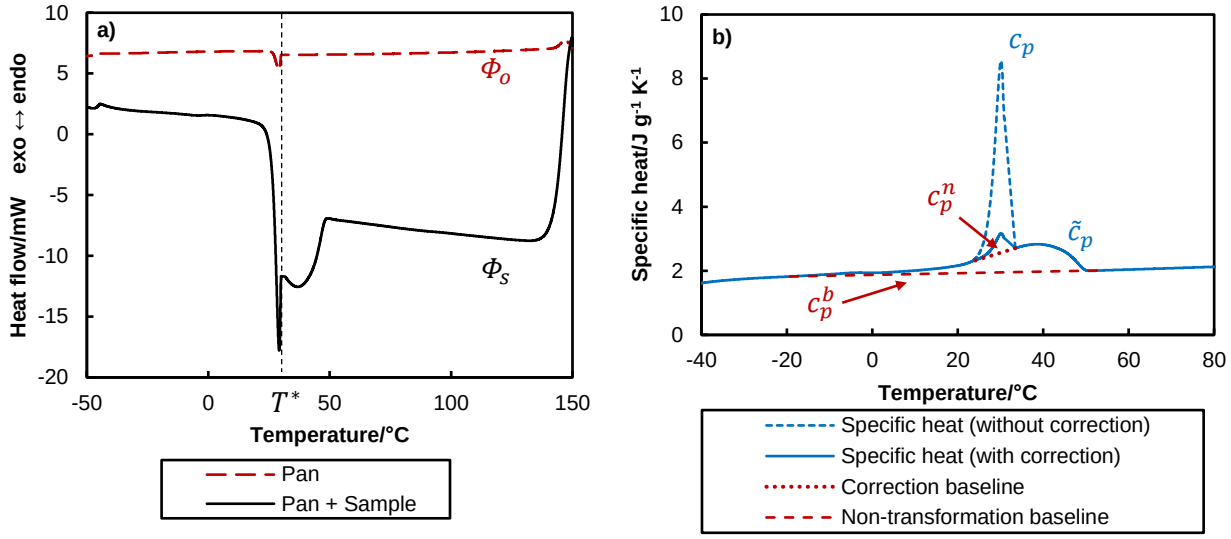

Fig. 2 a Heat flow measurement of a sample pan and the same sample pan with a wax-oil DSC sample (sample mass: 8.093 mg) with two sections of different cooling rates **b** Specific heat c_p peaking around T^* and its correction according to the correction baseline c_p^n.

With the as-defined temperature program, two scans are conducted respectively on an empty aluminum sample pan (heat flow denoted as Φ_o) and on the same sample pan containing the sample (heat flow denoted as Φ_s). An example of measured heat flow is presented in **Fig. 2a**. The specific heat can be obtained by normalization in **(6)**, within each of the two sections:

$$c_p = \begin{cases} \dfrac{\Phi_s - \Phi_o}{m\dot{T}_1} \; for\; T > T^* \\ \dfrac{\Phi_s - \Phi_o}{m\dot{T}_2} \; for\; T \leq T^* \end{cases} \quad \textbf{(10)}$$

When plotting the calculated c_p, there is a large peak at around T^* (see **Fig. 2b**). This is probably due to the perturbated signal recorded by the calorimeter immediately after the cooling rate change, at T^*. There are two possible reasons for the generation of this peak. First, the crystallization continues and accelerates around the temperature T^* after isokinetic cooling of $\dot{T}_1$. Second, the cooling rate change may lead to an instable thermal control of the calorimeter. As a matter of fact, such an instability can also be seen in the empty pan scan (see **Fig. 2a** dashed line). It is thus difficult to quantify the effect of each origin.

In order to mitigate this peak effect, a correction method is hereafter proposed. First, the correction specific heat $\tilde{c}_p$ is suggested through the introduction of a proportionality factor g:

$$\left(\tilde{c}_p - c_p^b\right) = g\left(c_p - c_p^n\right) for\; T \approx T^* \quad \textbf{(11)}$$

where c_p^b is the non-transformational specific heat which is determined similarly by a spline interpolation (red dashed line in **Fig. 2b**) ; c_p^n is the correction baseline around T^* by linear interpolation (red dotted line in **Fig. 2b**). The factor g is found by ensuring the same enthalpy of crystallization that is calculated by the corrected specific heat $\tilde{c}_p$ compared to isokinetic cooling scans:

$$\Delta H_{tr} = \int_{T_{WA}}^{T_{tr}^f} \left(\tilde{c}_p - c_p^b\right) dT \quad \textbf{(12)}$$

Similar to isokinetic scans, f_{SW} for non-isokinetic conditions can be calculated and used for further kinetics description:

$$f_{SW}(T) = \frac{\int_{T_{WA}}^{T} \left(\tilde{c}_p - c_p^b\right) dT}{\Delta H_{ref}} \quad \textbf{(13)}$$

4. Experimental

4.1. Materials

From the vast possible combinations of wax-oil mixtures, two materials that represent cosmetic wax-based mixtures have been chosen: a binary wax-oil mixture and a commercialized lipstick paste with similar total wax quantity. The binary mixture (noted as JN15-DEK) was prepared by mixing 15 wt% of a synthetic polyethylene wax Jeenate 3H (Jeen International Corporation, New Jersey, United States) in a hydrogenated poly-1-decene oil Dekanex 2006 FG (Jan Dekker, Amsterdam, the Netherlands) at 98 °C. The lipstick paste (noted as GL740) is the commercialized product Dior Addict Lacquer Stick Color 740, acquired directly from the industrial site (Parfums Christian Dior, Saint-Jean-de-Braye,

France). Both mixtures are chemically stable from -50 °C to 150 °C and were stored at room temperature before DSC tests. DSC scans show no liquid-solid transformation above -20 °C for oil components in both mixtures. According to the wax content and preliminary DSC tests, the reference enthalpies ΔH_{ref} for the two mixtures were determined: -222.9 J g^{-1} for JN15-DEK and -187.5 J g^{-1} for GL740.

4.2. Calorimetry scans

A power-compensated calorimeter DSC 8500 of Perkin Elmer was used. For each DSC scan, the sample was sealed in a 20 µL aluminum container. The sample mass should be neither too small to hide thermal signal to the baseline, nor too large to amplify the thermal inertia effect inside the sample. Without specifying, the sample mass is controlled within 4 to 10 mg.

4.2.1. Temperature calibrations

Two calibration methods were employed for isokinetic measurement conditions and non-isokinetic measurement conditions respectively.

For isokinetic conditions, the calorimeter was connected to a Liquid Nitrogen Cooling (CLN2) block for cooling rates from -20 °C min^{-1} to -200 °C min^{-1}. Preliminary calibrations with indium and lead standards were conducted for heating rates of 20, 50, 100, 150 and 200 °C min^{-1} by supposing the symmetry of heating and cooling on calorimeter thermal control.

For non-isokinetic conditions, the calorimeter was connected to an IntraCooler cooling block which allows a better cooling stability at lower cooling rates (from -5 to -50 °C min^{-1}). Temperature measurement was calibrated at a single cooling rate of 10 °C min^{-1}. A pre-determined temperature correction at different cooling rates was used for each DSC scans:

$$T_c = T_m + \left(10 - \dot{T}\right) * 0.03 \qquad \textbf{(14)}$$

T_c is the temperature after correction and T_m is the sample temperature which is measured by the calorimeter.

4.2.2. Isokinetic DSC scans

For isokinetic cooling conditions, constant cooling scans were conducted on both mixtures from 150 °C to -50 °C, with cooling rates of -20, -50, -100, -150 or -200 °C min^{-1}. The influence of thermal inertia was characterized on both mixtures with four different sample mass around 2, 5, 10 and 15 mg, at two cooling rates -20 and -200 °C min^{-1}. Repeatability studies and sensibility tests on sample mass were conducted using both mixtures at all mentioned cooling rates.

4.2.3. Non-isokinetic DSC scans

Non-isokinetic DSC scans were conducted on JN15-DEK with T^* programmed at 30 °C and GL740 with T^* programmed at 50 °C. Three combinations of $\left|\dot{T}_1\right|$-$\left|\dot{T}_2\right|$ were chosen for both samples: 50-20, 50-10 and 50-5. For corresponding non-isokinetic modelling, constant cooling rate scans were carried out, from 150 °C to -50 °C with cooling rates of -20, -10 and -5 °C min^{-1} on both samples. Constant cooling rate scans at -50 °C min^{-1} were not obtained because the cooling capacity was not efficient at low temperature (below 0 °C) at this cooling rate.

5. Results and Discussion

5.1. Isokinetic conditions

5.1.1. Influence of sample mass

Thermal inertia can be an important factor in fast cooling DSC technologies as reported [43]. At high cooling rate, the characteristic time for heat conduction inside the sample volume is essential for the detection of thermal signals. If the sample volume is larger, the characteristic conduction time will be larger (considering $x^2 = Dt$ with x the characteristic conduction distance, D the heat diffusion coefficient, and t the characteristic conduction time), and a more significant thermal delay can be observed consequently. This effect can be interpreted by cooling scans on different sample mass. We evaluated this inertia effect with two limit cooling rates, respectively -20 and -200 °C min^{-1}. The transformational specific heat, as deduced from the scans after treatment, are plotted in **Fig. 3**. The total enthalpy of crystallization ΔH_{tr} and the wax appearance temperature T_{WA} are chosen to indicate the influence of thermal inertia and are presented in **Table 1**.

For the cooling rate -20 °C min^{-1}, only small differences in specific heat profiles can be seen. As shown in **Fig. 3** and **Table 1**, there is only a small variation of ΔH_{tr} and T_{WA} for a sample mass lower than 10 mg. However, the crystallization peak (around 52 °C and 70 °C for JN15-DEK and GL740, respectively) is stronger and narrower for a small sample mass. This difference can be explained by a lower characteristic conduction distance for smaller samples. In a smaller sample, the temperature is more homogenous during crystallization. In this case, the phase transformation signal is captured in a shorter time duration. As for larger sample mass, the thermal signal is more likely to be an averaged value because the heat conduction inside the sample delays crystallization at the center.

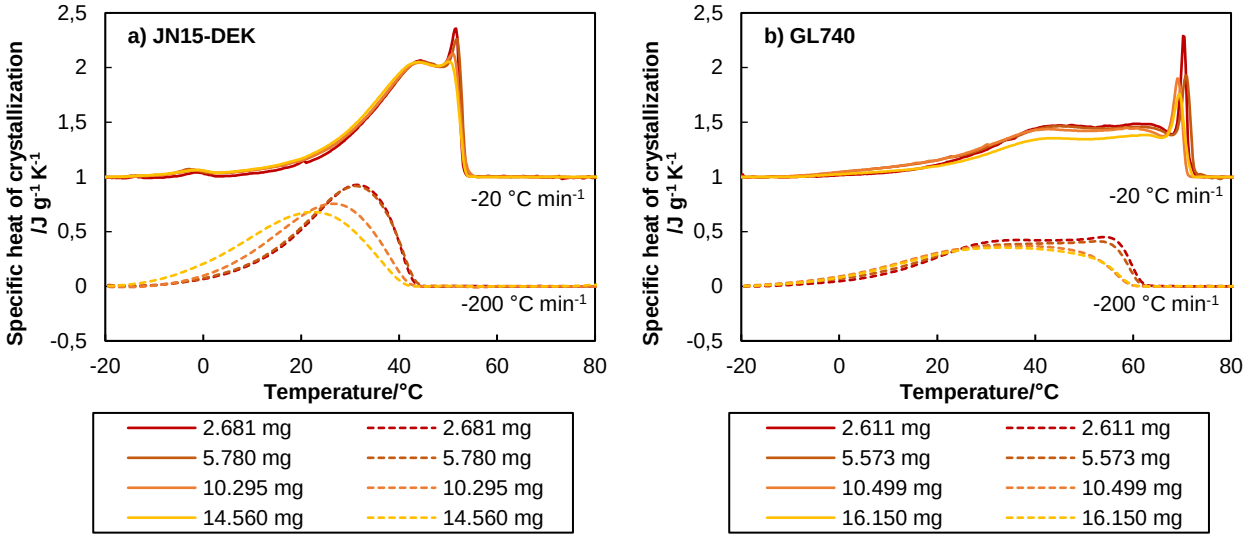

Fig. 3 Transformational specific heat profiles for samples **a** JN15-DEK and **b** GL740 at two cooling rates -20 °C min^{-1} and -200 °C min^{-1} with different sample mass. Specific heat profiles were shifted vertically for visualization reasons.

For the cooling rate -200 °C min^{-1}, as expected, the delay due to heat conduction is much more important, especially when the sample mass is large. The crystallization peak shifts significantly to lower temperatures when sample mass is greater than 10 mg, and the variation of ΔH_{tr} and T_{WA} is larger in this case. Enthalpy integration may lead to underestimated results of ΔH_{tr} for large sample mass because of the error introduced by heat control limit of the calorimeter. T_{WA} decreases with an increase in sample mass, due to the delay by thermal inertia. As it can be seen in **Fig. 3** and **Table 1**, the impact of sample mass on the variation of T_{WA} is less than 3 °C. This result reaffirms that the sample mass should be in a consistent range (4-10 mg).

Table 1 Influence of sample mass: total enthalpy of crystallization ΔH_{tr} and wax appearance temperature T_{WA} with different sample mass on two different cooling rates for JN15-DEK and GL740

	Cooling rate -20 °C min^{-1}		Cooling rate -200 °C min^{-1}	
Sample mass/mg	Total enthalpy of crystallization ΔH_{tr} /J g^{-1}	Wax appearance temperature T_{WA} /°C	Total enthalpy of crystallization ΔH_{tr} /J g^{-1}	Wax appearance temperature T_{WA} /°C
JN15-DEK				
2.681	-22.8	53.5	-21.0	43.2
5.780	-24.6	54.1	-21.2	43.7
10.295	-24.0	54.6	-19.1	43.2
14.560	-24.5*	53.7	-19.9*	41.1
GL740				
2.611	-21.8	72.4	-19.0	62.3
5.573	-22.7	73.2	-18.4	61.6
10.499	-21.6	71.1	-16.7	59.3
16.150	-18.2*	71.9	-15.8*	59.7

* Controlling the temperature program for large sample mass is difficult, especially at high cooling rate. As a result, the absolute value of enthalpy integration may be significantly underestimated.

5.1.2. Repeatability tests

Repeatability tests were conducted on both mixtures. For each material, three quasi-identical DSC samples were prepared with only slight differences on sample mass (JN15-DEK: 7.691 ± 0.259 mg and GL740: 5.639 ± 0.921 mg). For each DSC sample, isokinetic scans were conducted with cooling rates -20, -50, -100, -150 and -200 °C min^{-1}. The profiles of c_p^{tr} of each repeated test (see **Fig. 4**) shows no significant difference for both samples. Average value and uncertainty (by standard deviation) for total enthalpy of crystallization ΔH_{tr} and wax appearance temperature T_{WA} in each thermal condition were calculated and are given in **Table 2**. In general, an uncertainty of about ± 1 to ± 2 J g^{-1} on enthalpy of crystallization (corresponding to 5-10 % on relative value) can be introduced with our defined protocols of experimental measurement, baseline processing and integration. Uncertainty on wax appearance temperature in most cases is less than ± 1.5 °C. Without further elaborating in a vast combination of mixtures, we can considerer that there is an uncertainty of ± 10 % on ΔH_{tr} and ± 1.5 °C on T_{WA} with our protocols. This uncertainty level is considered adequate for our current experimental studies and kinetics modelling.

Table 2 Repeatability tests on JN15-DEK and GL740: Total enthalpy of crystallization ΔH_{tr} and wax appearance temperature T_{WA} at different cooling rates

	JN15-DEK		GL740	
Cooling rate $\dot{T}$ /°C min^{-1}	Total enthalpy of crystallization ΔH_{tr}/J g^{-1}	Wax appearance temperature T_{WA}/°C	Total enthalpy of crystallization ΔH_{tr}/J g^{-1}	Wax appearance temperature T_{WA}/°C
-20	-22.8 ± 2.0	54.7 ± 0.9	-19.7 ± 2.1	71.0 ± 0.3
-50	-22.9 ± 2.0	52.5 ± 1.5	-19.0 ± 0.6	68.4 ± 0.3
-100	-22.6 ± 1.9	49.2 ± 0.8	-19.8 ± 0.8	65.4 ± 0.3
-150	-21.9 ± 0.8	47.1 ± 0.7	-19.3 ± 0.2	63.8 ± 0.3
-200	-21.1 ± 0.4	43.3 ± 0.4	-18.5 ± 0.9	60.5 ± 0.4

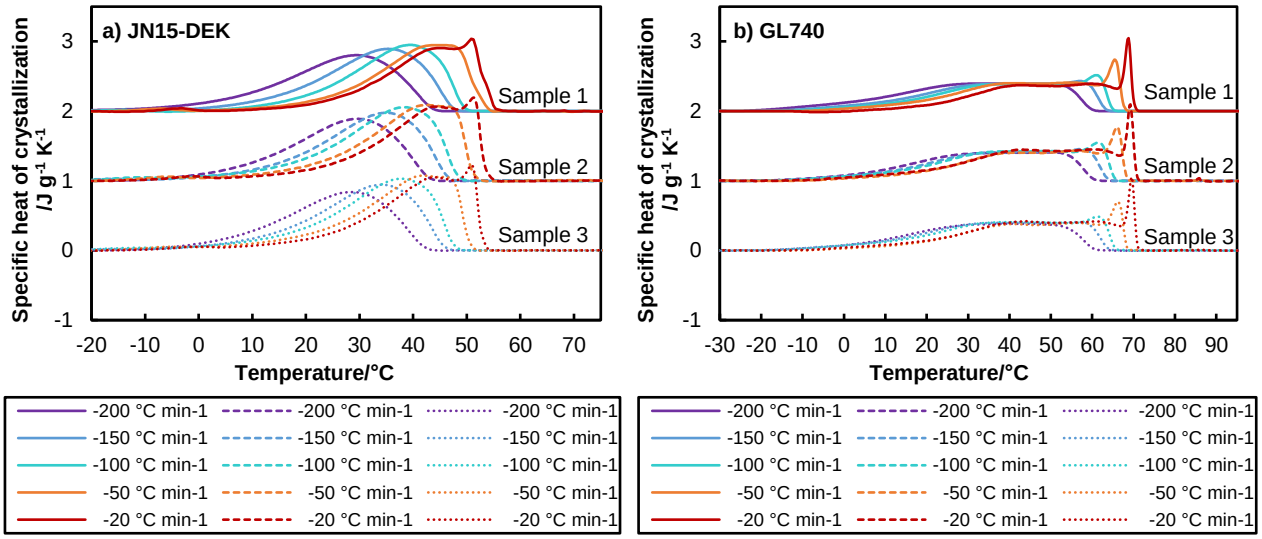

Fig. 4 Transformational specific heat profiles for **a** JN15-DEK and **b** GL740 at two cooling rates -20, -50, -100, -150 and -200 °C min^{-1} with three repeated scans. Specific heat profiles are shifted vertically for visualization reasons

5.1.3. Influence of cooling rate

The same repeatability results can be used to analyze the impact of cooling rates. According to specific heat profiles in **Fig. 4**, multiple crystallization peaks can be seen for lower cooling rates scans especially at -20 °C min^{-1}. This indicates an existence of different phase transformation mechanisms or components in complex wax-based mixtures. Understanding such phenomena could be laborious and will not therefore be the subject of the present study. At higher cooling rates, thermal signals become a result of an average of different phase transformation effects in a shorter time interval, so that the transformational specific heat profiles are found smoother.

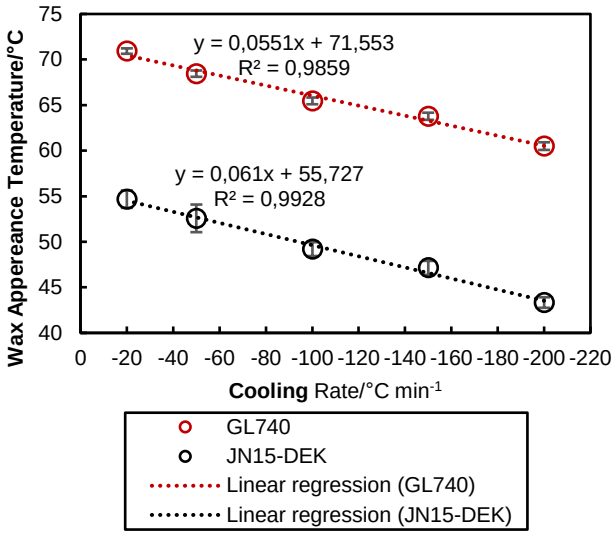

Fig. 5 Wax appearance temperature T_{WA} of JN15-DEK and GL740 plotted against the cooling rate

Another major impact of the cooling rate is about the temperature T_{WA}. When increasing the cooling rates, transformational specific heat profiles are found similar, but with a continuous shift to the lower temperatures. From -20 °C min^{-1} to -200 °C min^{-1}, the temperature difference can be up to 10 °C. Since the thermal inertia is unlikely to introduce such difference, the shift on T_{WA} is probably associated with the supercooling effect: at a higher cooling rate, a large supercooling is favorable and leads to a lower nucleation temperature. Specifically, as plotted in **Fig. 5**, the wax appearance temperature T_{WA} is correlated linearly to $\dot{T}$:

$$T_{WA}(\dot{T}) = T_{WA}^{o} + \alpha_T \dot{T} \qquad \textbf{(15)}$$

In this expression, T_{WA}^{o} is the temperature extrapolation to a fictional cooling rate of 0 °C min^{-1}, and can be considered as the thermodynamic equilibrium temperature for crystallization. This correlation is coherent with results obtained in several studies mentioned previously [11, 22, 24], while other studies suggest that the dependency is non-linear [12, 28, 29]. We believe that this dependency of T_{WA} on cooling rate might depend on the type of wax-oil combination. Without further research on other mixture systems, we will assume that for our cosmetic waxy mixtures, the temperature T_{WA} is linearly dependent on cooling rate at relatively high cooling rates ($\dot{T} \leq$ -20 °C min^{-1}). With a linear regression, the absolute value of the slope α_T are found 0.061 (min) and 0.055 (min) for JN15-DEK and GL740, respectively. Actually, α_T can be seen as the induction time for isokinetic cooling conditions, considering:

$$\alpha_T = -\left(T_{WA}^{o} - T_{WA}(\dot{T})\right)/\dot{T} \qquad \textbf{(16)}$$

Fig. 6 shows the plots of f_{SW} against temperature at different cooling rates. Coherent with what precedes, are recovered similar curves that shift towards lower temperatures at higher cooling rates. The final solid wax fractions converge at low temperatures, which is consistent to similar values of enthalpy of

crystallization ΔH_{tr} according to **Table 2**. These variations are probably due to the previously stated uncertainty. It should be noted that the final solid wax fraction of the two materials is lower than the total wax content (15 wt%). There remains probably dissolved wax in these mixtures, even after cooling down to very low temperatures for a full crystallization.

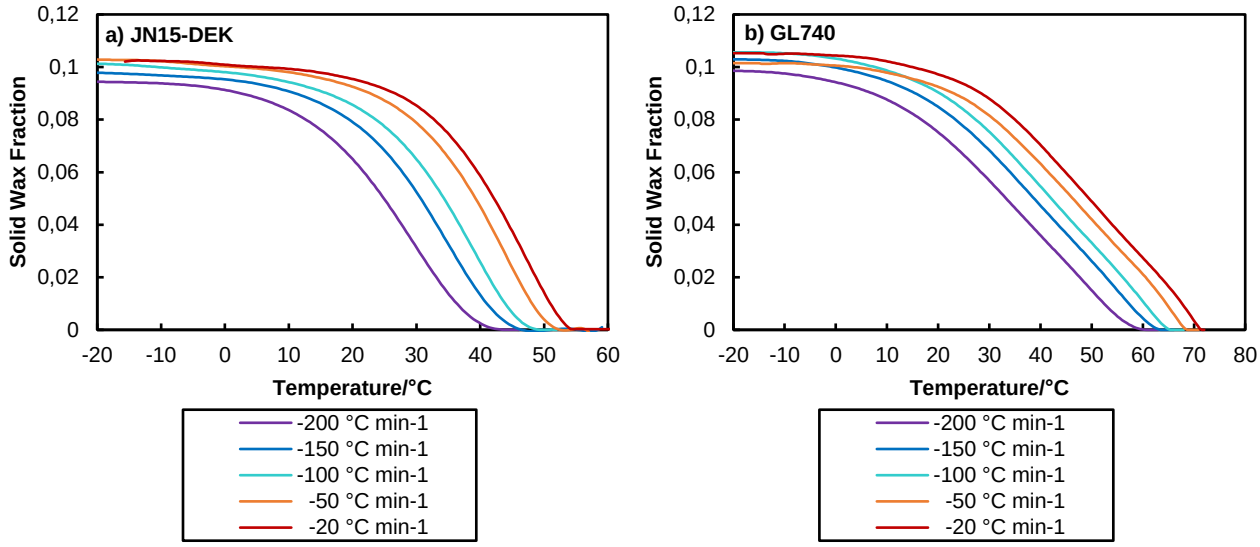

Fig. 6 Evolution of DSC-deduced solid wax fraction f_{SW} of **a** JN15-DEK and **b** GL740 at different cooling rates.

5.2. Non-isokinetic conditions

For non-isokinetic conditions, solid wax fraction profiles were calculated; they are plotted in **Fig. 7**. Isokinetic profiles of the same cooling rate $\dot{T}_2$ (cooling rate in the second cooling section) are also plotted for comparison. As expected, the same f_{SW} can be seen before reaching the cooling rate change temperature T^* (T^* is slightly higher after temperature correction). Below the temperature T^*, f_{SW} profiles shifted towards the corresponding cooling rate $\dot{T}_2$. There seems to be an "acceleration" of crystallization at the beginning of the cooling rate change: when applying a lower cooling rate $\dot{T}_2$, the crystallization rate increases when comparing to that of the isokinetic curve (slope change). f_{SW} tends to converge towards the same value as for isokinetic condition after cooling rate change. However, there may exist significant errors around T^* and globally. These errors could introduce unreasonable f_{SW} profiles, such as the excessive increase of f_{SW} in "50-5" profile for GL740. Due to experimental limits, we may conclude carefully that a decreasing cooling rate possibly increases crystallization quantity within the same temperature interval.

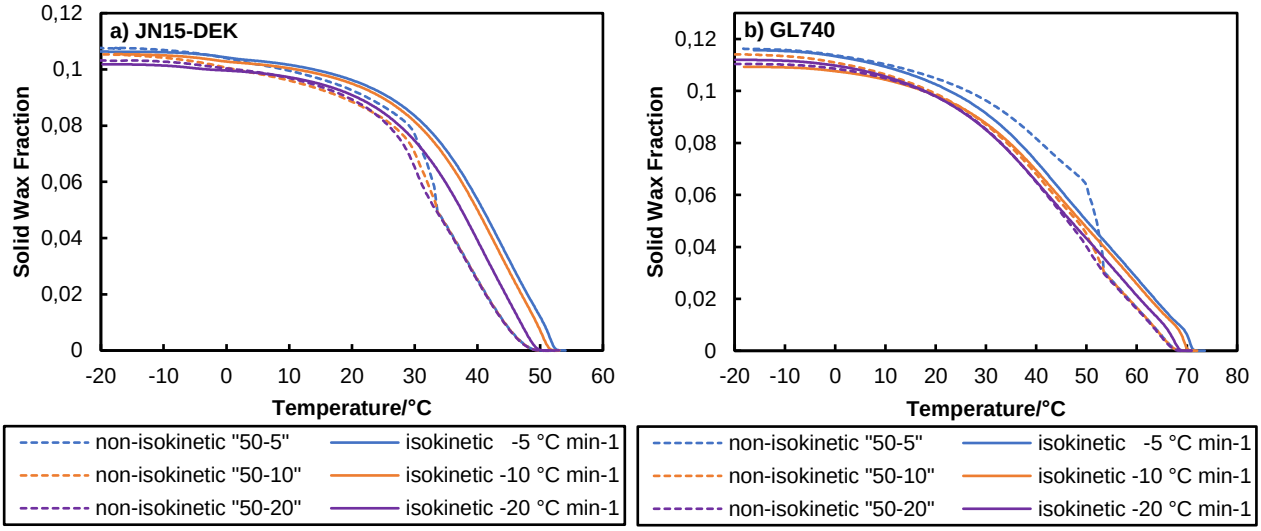

Fig. 7 Solid wax fraction f_{SW} for non-isokinetic scans for **a** JN15-DEK and **b** GL740 compared to isokinetic cooling scans of cooling rates $\dot{T}_2$

6. Kinetics Modelling

6.1. Isokinetic modelling

Based on experimental results, the kinetics model should include the induction effect and growth kinetics at different cooling conditions. The supercooling effect is significantly dependent on the cooling rate according to **Fig. 5** and should be considered in kinetics modelling. The modelling of induction effect can be referred to the linear dependency of T_{WA} to the cooling rate $\dot{T}$ which corresponds to the equation **(16)**. By using a constant $\hat{\alpha}_T$ (unit: min) which depends on the composition of the material, f_{SW} profiles can be shifted to a quasi-static cooling profile $f_{SW}\left(T - \hat{\alpha}_T\dot{T}, 0\right)$. Mathematically, the shift can be expressed by:

$$f_{SW}\left(T, \dot{T}\right) = f_{SW}\left(T - \hat{\alpha}_T\dot{T}, 0\right) \qquad \textbf{(17)}$$

With $\hat{\alpha}_T$ values of 0.090 min for JN15-DEK and 0.095 min for GL740, all shifted isokinetic f_{SW} profiles can be well superimposed in the intermediate f_{SW} zone, between 0.02 and 0.08 for both mixtures (**Fig. 8**). However, the curves are slightly diverging at lower solid wax fraction. This can be probably explained by different impacts of supercooling on growth kinetics which could be strongly associated to cooling rate in the early stage of the crystallization. Consequently, the values of $\hat{\alpha}_T$ are significantly different to those of α_T obtained by linear regressions in **Fig. 5**. At higher solid wax fraction, the profiles of f_{SW} are also slightly diverging vertically. This could be related to the uncertainty in enthalpy integration as previously discussed in subsection .

Initially, the growth kinetics was conducted on kinetics curves shown in **Fig. 8** by using the constant cooling rate Ozawa model. By approximating the volume fraction f_v to the fraction f_{SW}, the double logarithm form of the Ozawa model in equation **(4)** becomes thus:

$$ln\left[-ln\left(1-f_{SW}\left(T-\hat{\alpha}_T\dot{T},0\right)\right)\right]=ln[\chi(T)]-n\,ln|\dot{T}| \qquad \textbf{(18)}$$

Considering the quasi-overlapping kinetics curves of f_{SW} (as shown in **Fig. 8**), $n \approx 0$ can be obtained from the double logarithm plot based on equation **(18)**. As the value of the Avrami coefficient n is correlated to the dimension of the crystalline growth, a zero-value signifies that the crystalline growth is "dimensionless", which does not correspond to any physical meaning. Furthermore, if $n = 0$ is applied to the Ozawa's model, the equation **(4)** simply leads to the exponential of the fitting function $\chi(T)$: $f_{SW}\left(T-\hat{\alpha}_T\dot{T},0\right)=1-exp\left(-\chi(T)\right)$. For these reasons, it is believed that the classic Avrami-Ozawa model may not be suitable for kinetics modelling of wax-oil mixtures.

Here, we suggest a semi-empirical modelling approach by applying directly a master curve $\xi(T)$ to model the growth kinetics curves. The master curve $\xi(T)$ and the value of $\hat{\alpha}_T$ can be optimized by minimizing the cost function $L(f_{SW},\xi)$ according to the shifted kinetics curves in **Fig. 8**:

$$L(f_{SW},\xi)=\sum_{j,k}\left(f_{SW}\left(T^j-\hat{\alpha}_T\dot{T}^k,0\right)-\xi(T)\right)^2 \qquad \textbf{(19)}$$

In our study, $\xi(T)$ is fitted by a monotonic decreasing polynomial function in the transformation zone $T_{tr}^f \le T \le T_{tr}^i$, with $\xi\left(T=T_{tr}^f\right)=f_{SW}^{max}$ and $\xi\left(T=T_{tr}^i\right)=0$. Compared to classic kinetics models, the choice of polynomial form allows to describe the growth kinetics of mixtures potentially composed of several wax components that induces multiple temperature intervals of crystallization. For $T > T_{tr}^i$, the value of $\xi(T)$ is zero. And for $T < T_{tr}^f$, $\xi(T)=f_{SW}^{max}$. As shown in **Fig, 8**, the as-obtained master curves (dashed line) are well correlated to kinetics curves for both mixture samples.

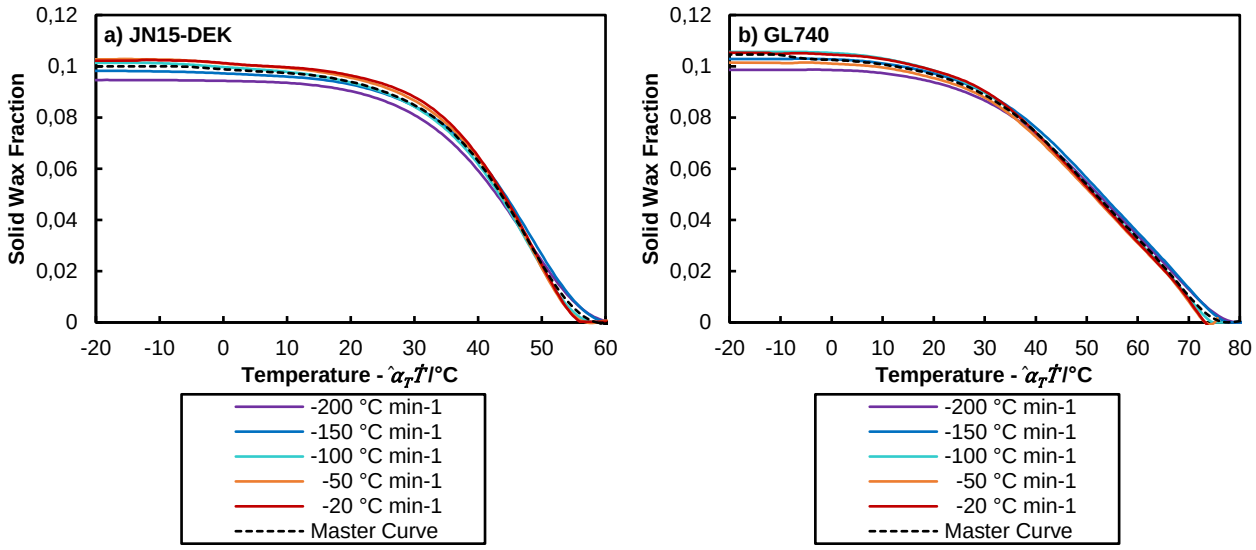

Fig. 8 Horizontally shifted solid wax fraction f_{SW} profiles (solid lines) with a shift factor of $-\hat{\alpha}_T\dot{T}$ for **a** JN15-DEK and **b** GL740 and the fitted master curve (dashed line)

Thus, the modelled solid wax fraction (denoted as $\hat{f}_{SW}$) for isokinetic conditions can be calculated by:

$$\hat{f}_{SW}(T,\dot{T}) = \xi(T - \hat{\alpha}_T \dot{T}) \quad \textbf{(20)}$$

Concerning isokinetic scans for both two mixtures, the modelling results show a good correlation with experimental results (**Fig. 9**). Only slight differences between experimental and modelling can be seen. We can validate our kinetic modelling in isokinetic conditions considering the probable measurement uncertainty of DSC.

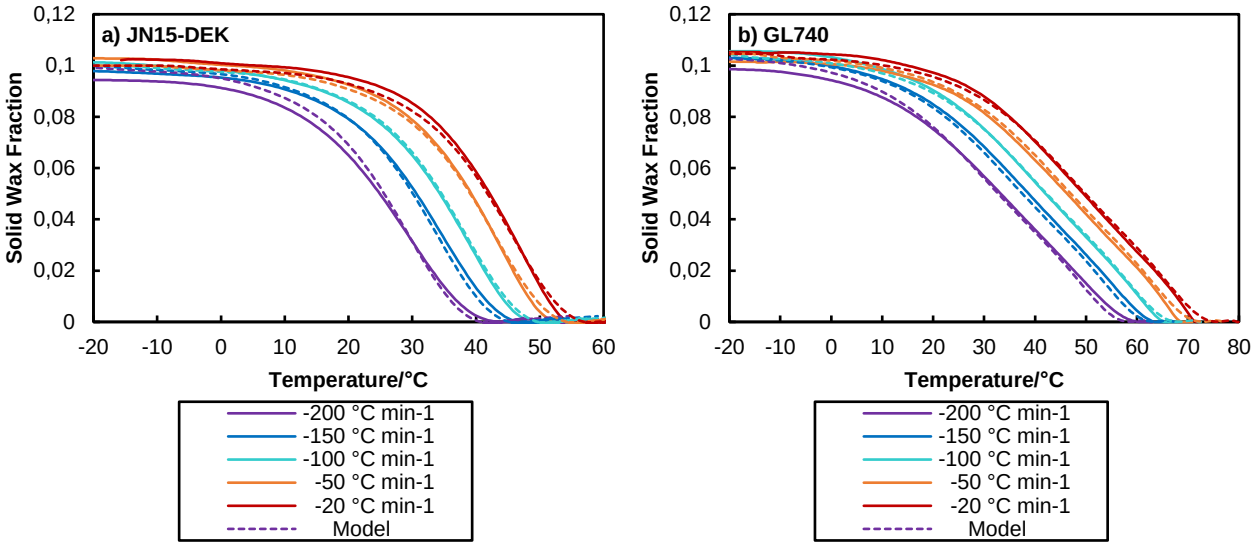

Fig. 9 Solid wax fraction profiles of **a** JN15-DEK and **b** GL740 calculated by experimental scans (solid lines) and modelling (dashed lines)

6.2. Non-isokinetic modelling

Regarding non-isokinetic conditions, we propose here a generalization of the isokinetic model **(20)** to non-isokinetic modelling. Three key points should be defined for non-isokinetic temperature profiles: a nucleation condition, a crystallization growth rate and then an end condition of the crystallization. It should be noted that thermal signals for crystallization and fusion in many wax-based materials are not symmetrical due to supercooling effect. Here the model will only deal with monotonic temperature decrease, which is the most common thermal condition in solidification processes.

6.2.1. Nucleation condition

For an isokinetic cooling condition, the modelled wax appearance temperature $\hat{T}_{WA}^{\dot{T}}$ can be written as:

$$\hat{T}_{WA}^{\dot{T}} = \hat{T}_{WA}^{o} + \hat{\alpha}_T \dot{T} \quad \textbf{(21)}$$

$\hat{T}_{WA}^{o}$ is the wax appearance temperature at $\dot{T} \to 0$, equivalent to the temperature T_{tr}^{i} that can be obtained experimentally.

Thermal history in non-isokinetic supercooling zone should be considered. Referring to Scheil's definition of the induction time of nucleation of non-isothermal conditions, as shown in **(3)**, the non-isokinetic wax appearance temperature $\hat{T}_{WA}$ can be calculated by the contribution of each temperature steps dT:

$$\int_{\hat{T}_{WA}^{0}}^{\hat{T}_{WA}} \frac{dT}{\hat{T}_{WA}^{\dot{T}} - \hat{T}_{WA}^{o}} = 1 \qquad \textbf{(22)}$$

By using **(20)**, this expression is simplified to:

$$\int_{\hat{T}_{WA}^{0}}^{\hat{T}_{WA}} \frac{dT}{\hat{\alpha}_T \dot{T}} = \int_{t_o}^{t_{WA}} \frac{dt}{\hat{\alpha}_T} = 1 \qquad \textbf{(23)}$$

where t_{WA} is the time when wax begins to crystallize and t_o is the time when the temperature reaches $\hat{T}_{WA}^{o}$. **(22)** is equivalent to:

$$t_{WA} = t_o + \hat{\alpha}_T \qquad \textbf{(24)}$$

As demonstrated, t_{WA} is independent of the thermal path. $\hat{\alpha}_T$ can be interpreted as the non-isokinetic supercooling induction time. The nucleation condition is thus a time delay of $\hat{\alpha}_T$ after reaching the temperature $\hat{T}_{WA}^{o}$.

6.2.2. Crystallization growth rate

Supposing the continuity of $\hat{f}_{SW}(T, \dot{T})$ in **(19)**, the total derivative of $\hat{f}_{SW}(T, \dot{T})$ can be written as:

$$d\hat{f}_{SW}(T, \dot{T}) = \frac{\partial}{\partial T}\xi(T - \hat{\alpha}_T \dot{T})dT + \frac{\partial}{\partial \dot{T}}\xi(T - \hat{\alpha}_T \dot{T})d\dot{T} \qquad \textbf{(25)}$$

The crystallization growth rate $d\hat{f}_{SW}(T, \dot{T})/dt$ is then:

$$\frac{d\hat{f}_{SW}(T, \dot{T})}{dt} = \xi'(T - \hat{\alpha}_T \dot{T}) \cdot [\dot{T} - \hat{\alpha}_T \ddot{T}] \qquad \textbf{(26)}$$

where ξ' is the first order derivative of ξ (or the local slope of ξ in **Fig. 8**), and $\ddot{T}$ is the second derivative of temperature T with respect to time. For isokinetic conditions, $\ddot{T}$ = 0 (no change in cooling rate) and equation **(25)** is then reduced to the time derivative of isokinetic form **(19)**. While the cooling rate $\dot{T}$ becomes smaller, $\ddot{T}$ will contribute to an increase of crystallization growth rate (considering $\ddot{T} > 0$, $\hat{\alpha}_T > 0$ and $\xi' < 0$), which may explain the "acceleration" phenomenon around the cooling rate change temperature T^* as previously discussed.

6.2.3. End condition

Wax crystallization is considered completed when $\hat{f}_{SW}$ reaches the final solid wax fraction f_{SW}^{max} according to DSC-measured isokinetic enthalpy: $f_{SW}^{max} = \Delta H_{tr}/\Delta H_{ref}$. A further cooling should not change the value of $\hat{f}_{SW}$.

6.2.4. Algorithm and modelling results

According to the definition of three elements of the kinetic model, an incremental algorithm can be resumed in the flow chart **Fig. 10**. The algorithm calculates the evolution of $\hat{f}_{SW}$ according to the thermal conditions at the time increment t^j. If the temperature of the increment T^j is lower than the temperature $\hat{T}_{WA}^{o}$, the mixture is in a metastable supercooling state. The beginning of the crystallization

growth is a time delay $\hat{\alpha}_T$ after reaching the temperature $\hat{T}^o_{WA}$. After nucleation, the crystalline growth increment corresponds to the multiplication of the growth rate $d\hat{f}_{SW}/dt$ that can be calculated from equation **(26)** and the time step Δt^j . If the updated incremental solid wax fraction $\hat{f}^j_{SW}$ is equal or greater to the f^{max}_{SW}, the crystallization process can be then considered complete. The suggested algorithm can be used for kinetics modelling of DSC results. Besides, it can be furthermore implemented in Finite Element Method (FEM) based simulations to calculate local crystallization kinetics.

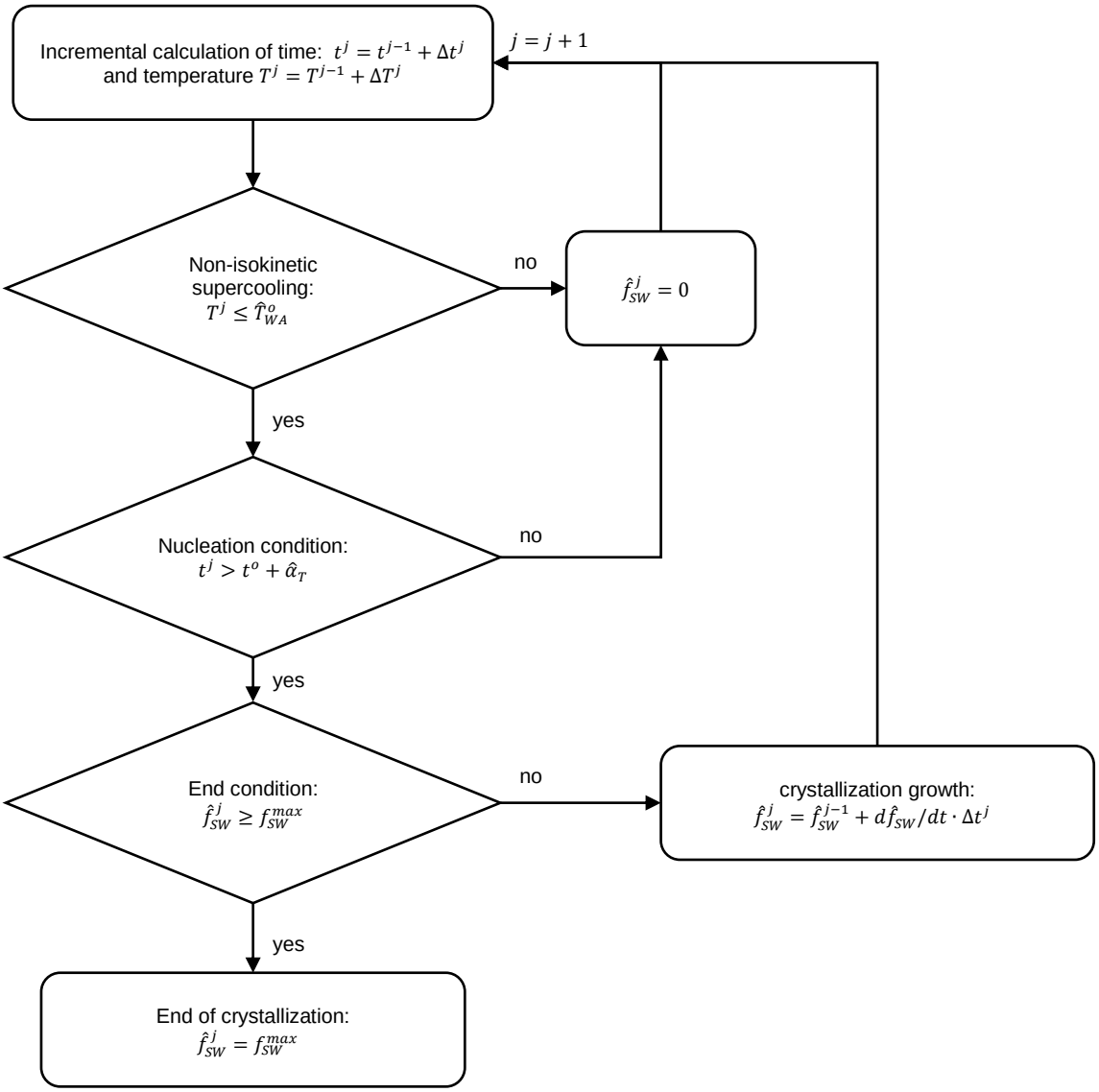

Fig. 10 Incremental calculation flow chart based on the proposed kinetic modelling of crystallization

With the as-proposed algorithm, non-isokinetic modelling was conducted on thermal condition of the "50-10" temperature program. The temperature profile was smoothed around T^* at the cooling rate

change time, to avoid abrupt variation of $\ddot{T}$ (**Fig. 11**). The smoothed curve was only slightly different from the temperature program around T^*.

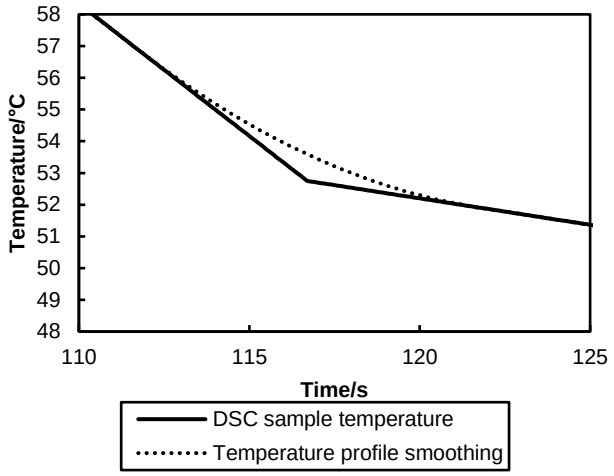

Fig. 11 Smoothen of modelling temperature around T^* for non-isokinetic condition "50-10" (example of T^* around 50 °C)

Fig. 12 globally shows a good correlation on the tendency between non-isokinetic modelling and experimental results. The model is capable to capture a local slope change of the solid wax fraction when cooling slows down, as seen in **Fig. 12a** around 30 °C and in **Fig. 12b** around 50 °C. However, modelling results (dotted lines) for both samples show significant differences to DSC measurements (dashed lines), mostly during the first cooling section above T^*. It is to be noticed that the baseline correction and the integration may affect the kinetics calculation for both sections. Considering the limits of current DSC technologies on non-constant cooling rate scans, we are unfortunately not able to evaluate precisely our non-isokinetic modelling.

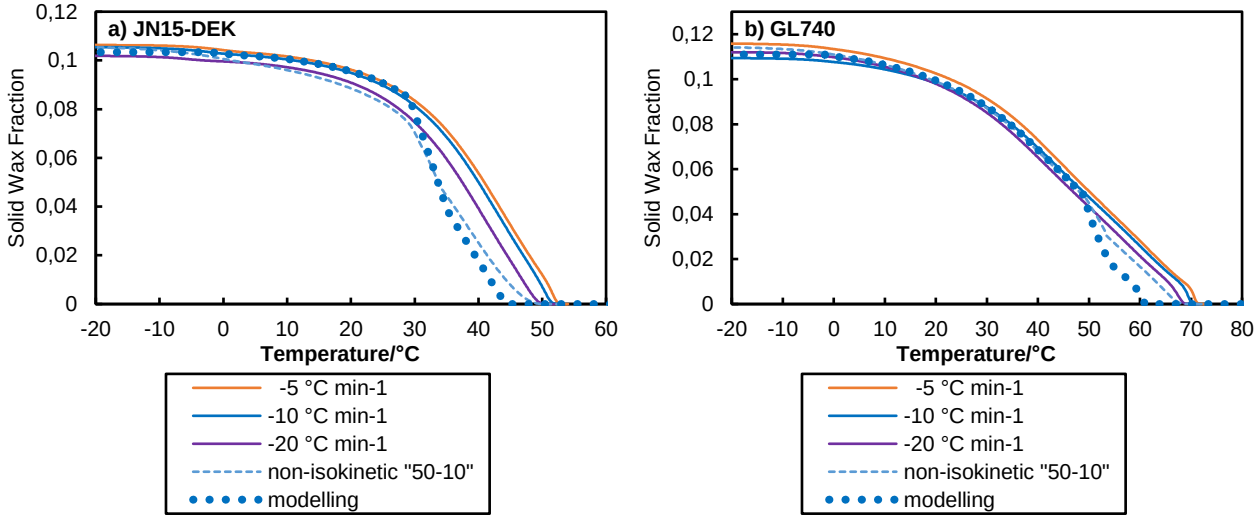

Fig. 12 Modelling of non-isokinetic condition "50-10" for **a** JN15-DEK and **b** GL740; isokinetic experimental results are shown for comparison

7. Conclusion

Crystallization kinetics of two representative wax-oil mixtures JN15-DEK and GL740 were characterized by DSC with different constant cooling rates from -20 °C min^{-1} to -200 °C min^{-1}, and with simplified non-isokinetic cooling conditions composed of two different constant rate cooling sections. It can be concluded that the cooling rate has a significant impact on the supercooling and on the wax appearance temperature T_{WA} that is linearly dependent on the cooling rate $\dot{T}$. The enthalpy of crystallization and kinetics profiles are merely influenced by the cooling rate.

Based on experimental results, a semi-empirical model was developed for kinetics modelling as an alternative of the Avrami-Ozawa theory. The kinetics model was expanded to non-isokinetic conditions with a differential form which can be further implementation in FEM-based calculations. A good correlation with experimental results was found, especially for isokinetic cooling scans. However, as far as we know, current commercialized DSC are incompatible for non-constant cooling rate conditions, which limits a more precise validation of our kinetics model in non-isokinetic conditions. We hope that future calorimetry development that enables non-isokinetic cooling will help us understand crystallization kinetics in industrial conditions.

Acknowledgement

The authors would like to acknowledge the financial support provided by Parfums Christian Dior.

Conflicts of Interest

The authors declare that there is no conflict of interest.

References

1. Dorset DL. Crystallography of the polymethylene chain: an inquiry into the structure of waxes. Oxford University Press; 2005.

2. Kané M, Djabourov M, Volle J-L. Rheology and structure of waxy crude oils in quiescent and under shearing conditions. Fuel. 2004; https://doi.org/10.1016/j.fuel.2004.01.017

3. Blake AI, Co ED, Marangoni AG. Structure and physical properties of plant wax crystal networks and their relationship to oil binding capacity. J Am Oil Chem Soc. 2014; https://doi.org/10.1007/s11746-014-2435-0

4. Blake AI, Marangoni AG. The use of cooling rate to engineer the microstructure and oil binding capacity of wax crystal networks. Food Biophys. 2015; https://doi.org/10.1007/s11483-015-9409-0

5. Abdallah DJ, Sirchio SA, Weiss RG. Hexatriacontane organogels. The first determination of the conformation and molecular packing of a low-molecular-mass organogelator in its gelled state. Langmuir. 2000; https://doi.org/10.1021/la000730k

6. Hwang H-S, Kim S, Singh M, Winkler-Moser JK, Liu SX. Organogel formation of soybean oil with waxes. J Am Oil Chem Soc. 2012; https://doi.org/10.1007/s11746-011-1953-2

7. Abdallah DJ, Weiss RG. Organogels and low molecular mass organic gelators. Adv Mater; 2000. https://doi.org/10.1002/1521-4095(200009)12:17<1237::AID-ADMA1237>3.0.CO;2-B

8. Baki G, Alexander KS. Introduction to cosmetic formulation and technology. Hoboken: John Wiley & Sons; 2015.

9. Venkatesan R, Nagarajan NR, Paso K, Yi Y-B, Sastry AM, Fogler HS. The strength of paraffin gels formed under static and flow conditions. Chem Eng Sci. 2005; https://doi.org/10.1016/j.ces.2005.02.045

10. Henaut I, Betro B, Vinay G. Differential scanning calorimetry contribution to a better understanding of the aging of gelled waxy crude oils. Oil Gas Sci Technol. 2019; https://doi.org/10.2516/ogst/2018095

11. Kasumu AS, Arumugam S, Mehrotra AK. Effect of cooling rate on the wax precipitation temperature of "waxy" mixtures. Fuel. 2013; https://doi.org/10.1016/j.fuel.2012.09.036

12. Ruwoldt J, Kurniawan M, Oschmann H-J. Non-linear dependency of wax appearance temperature on cooling rate. J Pet Sci Eng. 2018; https://doi.org/10.1016/j.petrol.2018.02.011

13. Andrade DEV, Marcelino Neto MA, Negrão COR. Non-monotonic response of waxy oil gel strength to cooling rate. Rheol Acta. 2018; https://doi.org/10.1007/s00397-018-1108-6

14. Morales-Rueda JA, Dibildox-Alvarado E, Charó-Alonso MA, Weiss RG, Toro-Vazquez JF. Thermo-mechanical properties of candelilla wax and dotriacontane organogels in safflower oil. Eur J Lipid Sci Technol. 2009; https://doi.org/10.1002/ejlt.200810174

15. Alvarez-Mitre FM, Morales-Rueda JA, Dibildox-Alvarado E, Charó-Alonso MA, Toro-Vazquez JF. Shearing as a variable to engineer the rheology of candelilla wax organogels. Food Res Inter. 2012; https://doi.org/10.1016/j.foodres.2012.08.025

16. Starink MJ. Analysis of aluminium based alloys by calorimetry: quantitative analysis of reactions and reaction kinetics. Inter Mater Rev. 2004; https://doi.org/10.1179/095066004225010532

17. Bogoeva-Gaceva G, Janevski A, Grozdanov A. Crystallization and melting behavior of iPP studied by DSC. J Appl Polym Sci. 1998; https://doi.org/10.1002/(SICI)1097-4628(19980118)67:3<395::AID-APP2>3.0.CO;2-H

18. Coccorullo I, Pantani R, Titomanlio G. Crystallization kinetics and solidified structure in iPP under high cooling rates. Polymer. 2003; https://doi.org/10.1016/S0032-3861(02)00762-0

19. Menczel JD, Judovits L, Prime RB, Bair HE, Reading M, Swier S. Differential scanning calorimetry. In: Menczel JD, Prime RB, editors. Thermal analysis of polymers: fundamentals and applications. Hoboken: John Wiley & Sons; 2009. pp. 7–239.

20. Cartledge HCY, Baillie CA. Studies of microstructural and mechanical properties of nylon/glass composite Part I The effect of thermal processing on crystallinity, transcrystallinity and crystal phases. J Mater Sci. 1999; https://doi.org/10.1023/A:1004713200894

21. Cantor B. Differential scanning calorimetry and the advanced solidification processing of metals and alloys. J Therm Anal. 1994. https://doi.org/10.1007/BF02546740

22. Ahmadi Khoshooei M, Fazlollahi F, Maham Y, Hassan A, Pereira-Almao P. A review on the application of differential scanning calorimetry (DSC) to petroleum products: wax crystallization study and structural analysis. J Therm Anal Calorim. 2019; https://doi.org/10.1007/s10973-019-08022-0

23. Baltzer Hansen A, Larsen E, Batsberg Pedersen W, Nielsen AB, Rønningsen HP. Wax precipitation from North Sea crude oils. 3. Precipitation and dissolution of wax studied by differential scanning calorimetry. Energy Fuels. 1991; https://doi.org/10.1021/ef00030a021

24. Zhao Y, Paso K, Sjöblom J. Thermal behavior and solid fraction dependent gel strength model of waxy oils. J Therm Anal Calorim. 2014; https://doi.org/10.1007/s10973-014-3660-3

25. Pan S, Germann N. Thermal and mechanical properties of industrial benchmark lipstick prototypes. Thermochim Act. 2019; https://doi.org/10.1016/j.tca.2019.178332

26. Padar S, Jeelani SAK, Windhab EJ. Crystallization kinetics of cocoa fat systems: experiments and modeling. J Am Oil Chem Soc. 2008; https://doi.org/10.1007/s11746-008-1312-0

27. Fernandes VA, Müller AJ, Sandoval AJ. Thermal, structural and rheological characteristics of dark chocolate with different compositions. J Food Eng. 2013; https://doi.org/10.1016/j.jfoodeng.2012.12.002

28. Paso KG, Senra M, Yi Y, Sastry AM, Fogler HS. Paraffin polydispersity facilitates mechanical gelation. Ind Eng Chem Res. 2005; https://doi.org/10.1021/ie050325u

29. Adhvaryu A, Erhan SZ, Perez JM. Wax appearance temperatures of vegetable oils determined by differential scanning calorimetry: effect of triacylglycerol structure and its modification. Thermochim Acta. 2002; https://doi.org/10.1016/S0040-6031(02)00180-6

30. Zougari MI, Sopkow T. Introduction to crude oil wax crystallization kinetics: process modeling. Ind Eng Chem Res. 2007; https://doi.org/10.1021/ie061002g

31. Avrami M. Kinetics of phase change. I General theory. J Chem Phys. 1939; https://doi.org/10.1063/1.1750380

32. Marangoni AG. Kinetics of crystal growth using the avrami model and the chemical potential approach. In: Marangoni AG. Kinetic analysis of food systems. New York: Springer, 2017. pp. 113-134.

33. Qiao JC, Pelletier JM. Crystallization kinetics in Cu46Zr45Al7Y2 bulk metallic glass by differential scanning calorimetry (DSC). J Non-Cryst Solids. 2011; https://doi.org/10.1016/j.jnoncrysol.2010.12.071

34. Nakamura K, Katayama K, Amano T. Some aspects of nonisothermal crystallization of polymers. II. Consideration of the isokinetic condition. J Appl Polym Sci. 1973; https://doi.org/10.1002/app.1973.070170404

35. Ozawa T. Kinetics of non-isothermal crystallization. Polymer. 1971; https://doi.org/10.1016/0032-3861(71)90041-3

36. Billon N, Barq P, Haudin J. Modelling of the cooling of semi-crystalline polymers during their processing. Inter Polymer Process. 1991; https://doi.org/10.3139/217.910348

37. Piorkowska E, Galeski A, Haudin J-M. Critical assessment of overall crystallization kinetics theories and predictions. Prog Polym Sci. 2006; https://doi.org/10.3139/217.910348

38. Shepilov MP, Baik DS. Computer simulation of crystallization kinetics for the model with simultaneous nucleation of randomly-oriented ellipsoidal crystals. J Non-Cryst Solids. 1994; https://doi.org/10.1016/0022-3093(94)90350-6

39. Blake AI, Marangoni AG. Plant wax crystals display platelet-like morphology. Food Struct. 2015; https://doi.org/10.1016/j.foostr.2015.01.001

40. Scheil E. Anlaufzeit der Austenitumwandlung. Archiv für das Eisenhüttenwesen. 1935; https://doi.org/10.1002/srin.193500186

41. Chan TW, Isayev AI. Quiescent polymer crystallization: Modelling and measurements. Polym Eng Sci. 1994; https://doi.org/10.1002/pen.760340602

42. Batsberg Pedersen W, Baltzer Hansen A, Larsen E, Nielsen AB, Rønningsen HP. Wax precipitation from North Sea crude oils. 2. Solid-phase content as function of temperature determined by pulsed NMR. Energy Fuels. 1991; https://doi.org/10.1021/ef00030a020

43. Vanden Poel G, Mathot VBF. High-speed/high performance differential scanning calorimetry (HPer DSC): Temperature calibration in the heating and cooling mode and minimization of thermal lag. Thermochim Acta. 2006; https://doi.org/10.1016/j.tca.2006.02.022